Performance analysis of a supersonic ejector cycle working with R245fa

Performance analysis of a supersonic ejector cycle working with R245fa

Federico Mazzelli, Adriano Milazzo*
University of Florence, Department of Industrial Engineering
via di Santa Marta, 3 – 50139 FIRENZE (ITALY)

Abstract

A supersonic ejector chiller for industrial use is currently being developed and tested as part of a project cooperation between Frigel s.p.a and DIEF (Department of Industrial Engineering, University of Florence). The refrigerator was built following a "ready to market" setup criterion and is intended for applications on the industrial refrigeration market or in air conditioning. The plant has a nominal cooling power of 40 kW and is powered by low temperature heat (from 90 up to 100 °C). The ejector is equipped with a movable primary nozzle and 9 static pressure probes along the mixing chamber/diffuser duct. The working fluid is R245fa. An extensive numerical campaign was performed to analyze the internal dynamics of the ejector. All the simulations were carried out by accounting for the real gas properties of the refrigerant. Comparison with experimental data resulted in close agreement both in terms of global and local parameters. Analyses showed that in order to achieve an accurate matching with the experimental data, it is necessary to correctly account for the surface roughness of the ejector. This is especially true for off-design operating conditions.

Keywords: Ejector chiller, CFD, R245fa, heat powered refrigeration, supersonic ejector

Nomenclature

B	Bias or systematic error of a measured quantity	*Greek:*	
h	Specific enthalpy, kJ kg^{-1}	θ	Sensitivity index
K	Roughness height, m	*Subscripts:*	
$\dot{m}$	Mass flow rate, kg s^{-1}	a	Arithmetic average
P	Precision index or random error of a measured quantity	p	Primary flow
$\dot{Q}$	Heat flux, W	rms	Root mean square
R	Derived quantity	s	Secondary flow or sand-grain
t	Student's t estimator	sg	Sand-grain roughness
U	Total uncertainty of a measured quantity	95%	Level of confidence in the uncertainty
$\dot{W}$	Power input, W	*Abbreviations:*	
x	Measured quantity	ER	Entrainment Ratio
$\bar{x}$	Average of a measured quantity	COP	Coefficient of Performance

* Corresponding author: adriano.milazzo@unifi.it – 0039 055 4796333

1. Research background

Constant increase in refrigeration demand calls for new, economical and environmentally safe technologies. In this context, ejector refrigeration is a promising solution in the light of its ability to utilize low temperature heat to produce cooling. This important feature makes it appealing for the industrial and automotive field in waste-heat recovery applications. Alternatively, it might enter the residential and commercial sector as an air conditioning device powered by solar energy. However, among heat-driven refrigerators, absorption cooling is by far the most established and competitive option, due to its high efficiency. Although ejector refrigerators are still quite far from the performance obtained by double-effect absorption cycle machines, nevertheless they can offer an effective alternative in all cases where simplicity, reliability and low investment costs are required. Compared with lithium-bromide/water absorption refrigerators, ejector cycles require fewer heat exchangers and do not suffer from problems of internal corrosion and crystallization of the solution (Srikhirin et al., 2001). Ammonia/water absorption refrigerators, on the other hand, use a toxic fluid, while ejector chillers may operate on various fluids and non-toxic, non flammable and environmentally safe options may be found. These advantages potentially offer significant savings due to lower capital and life-cycle maintenance costs. Hence, ejector refrigeration can play a significant role in the wide and hopefully increasing market of heat-driven refrigerators, provided that an adequate level of efficiency is reached.

In order to improve the performance of the chiller, optimization of the supersonic ejector is most important. The common practice is to design the ejector following empirical prescriptions (e.g. ESDU, 1986). A different paradigm was adopted for the prototype described herein. The ejector profile was designed following theoretical criteria and optimized by means of numerical simulations (more details are given in section 2.1). The commonly adopted ideal gas assumption (e.g., Ruangtrakoon et al., 2012, Sriveerakul et al., 2007) was released in this study and real gas behaviour was assumed in all simulations.

Furthermore, examples can be found in the literature for which the numerical simulations correctly reproduce mass flow rates at on-design operations but fail to predict the onset of off-design conditions (Varga et. al., 2011; Sriveerakul et. al., 2007). The present analysis suggests that better agreement could be achieved, provided that the impact of friction losses is correctly evaluated. To the authors' knowledge, this latter point has never been investigated in the relevant literature.

Finally, the reliability and robustness of any type of chiller should be tested in real working condition. The research described in this study, which involved both our university and an industrial partner, was conceived as a "demonstration of prototype chiller working in an operational environment" (i.e., Technology Readiness Level around 6 or 7).

A scheme and a thermodynamic cycle of the ejector refrigerator are shown in Fig. 1. Operation is similar to that of a conventional vapour compression machine, except the mechanical compressor is replaced by a liquid feed-pump, vapour generator and supersonic ejector. A detailed analysis of the cycle has been given by many different authors (e.g., Ginoux, 1973; Addy et al., 1981) hence, just a brief description is here given. The motive primary stream arriving from the generator (high pressure and temperature – point G) flows through a de Laval nozzle and accelerates till supersonic speed. As it enters the mixing chamber, the primary flow entrains the secondary fluid coming from the evaporator at state E. The two streams mix and kinetic energy is transferred from the primary to the secondary flow. Subsequently, the mixed stream is compressed as it flows through the diffuser section of the ejector and enters the condenser at point C. The condensate is then split into two currents: one is expanded through a throttling valve and fed back to the evaporator whilst the other is returned via a feed pump to the boiler. Basically, the whole cycle can be seen as composed of two parts, the power and refrigeration cycles. The energy exchange between the two parts occurs by means of a supersonic ejector, which is the core device of the refrigerator. The two cycles share the condenser, which has to transfer both motive and cooling power to the environment.

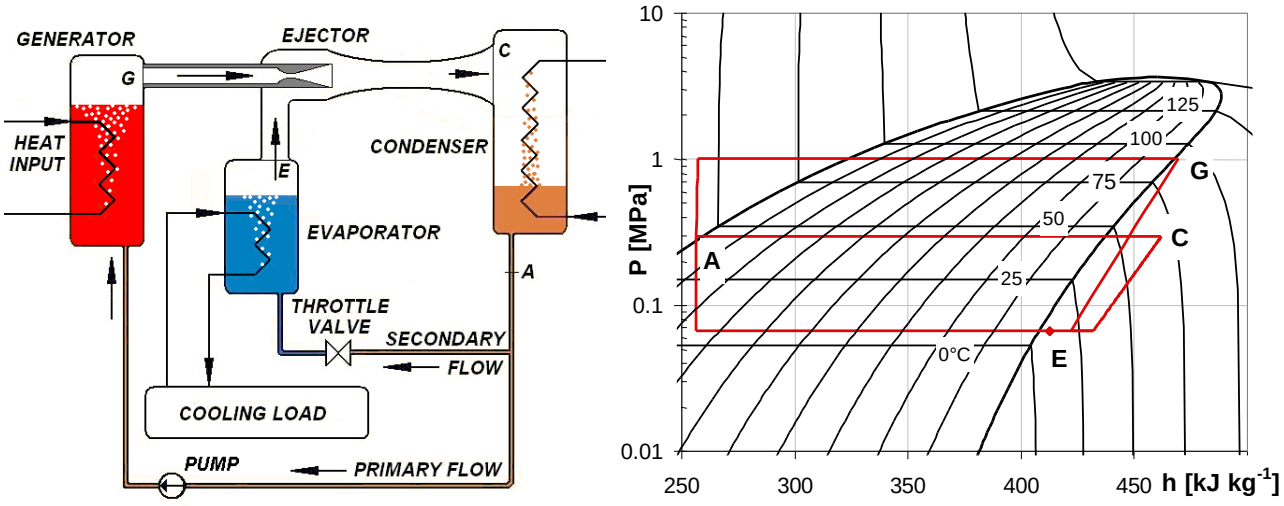

Fig. 1 – Schematics of the ejector refrigeration system and thermodynamic cycle

System performance can be quantified by means of the Coefficient Of Performance (COP). This is defined as the cooling load divided by the total heat and power inputs:

$$COP = \frac{\dot{Q}_{refr}}{\dot{Q}_{gen} + \dot{W}_{pump}} = \frac{\dot{m}_s}{\dot{m}_p} \frac{(h_E - h_A)}{(h_G - h_A)} \tag{1}$$

where the ratio between secondary to primary mass flow rate defines the Entrainment Ratio:

$$ER = \frac{\dot{m}_s}{\dot{m}_p} \tag{2}$$

Fig. 2 shows a typical supersonic ejector operating curve obtained at fixed evaporator and generator conditions and varying outlet pressure. The ejector's operation is said to be ''on-design" or in "chocked regime" when the mixed flow in the mixing chamber/diffuser reaches supersonic speed. Under these conditions the quantity of entrained suction flow is independent of the discharge pressure and the Entrainment Ratio (ER) is maximum. On the contrary, if the secondary flow is subsonic, the amount of suction flow drawn into the ejector depends on the outlet pressure and the operation is said to be ''off-design". The value of discharge pressure separating these two operation zones is called "critical pressure".
A change in evaporator and generator conditions leads to substantial modifications in ER and critical pressure. When the evaporator temperature is raised (i.e., moving from $T_{eva\text{-}1}$ towards $T_{eva\text{-}3}$ in Fig. 2), the ER increases as a consequence of the greater secondary mass flux. Higher saturation temperatures of the evaporator lead also to greater critical pressures (due to the higher total pressure of the suction flow). When increasing the generator pressure (i.e., moving from $T_{gen\text{-}1}$ towards $T_{gen\text{-}2}$ in Fig. 2), the increase in primary mass flow rate is not followed by a higher entrainment of the secondary stream, whose mass flow rate remains approximately constant (Bartosiewicz et al., 2005). Consequently, the ER is reduced. However, the greater energy content introduced by the motive flow allows for higher back pressures, thus increasing the critical pressure.

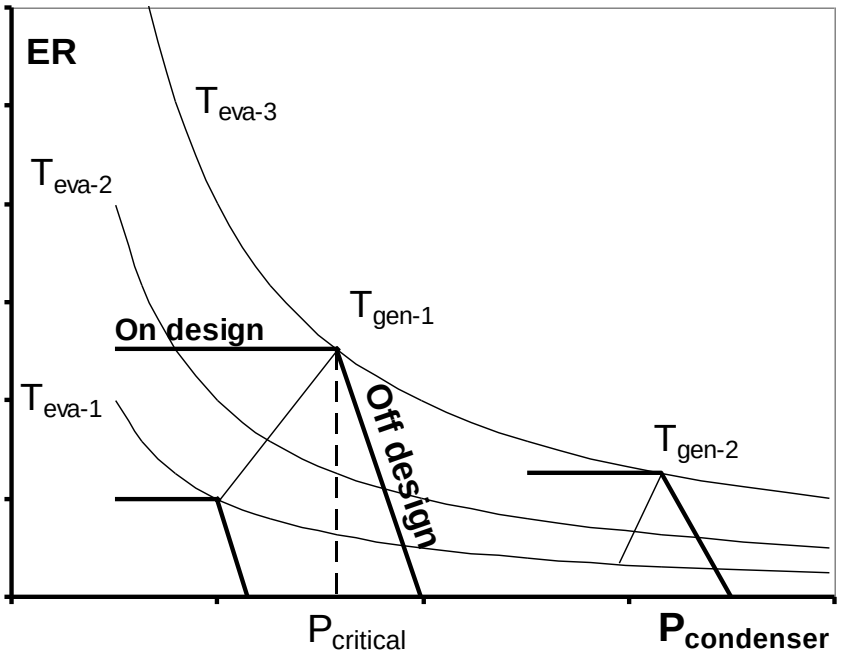

Fig. 2 – Typical ejector operating curve

2. Experimental apparatus

The main components of the present refrigerator are the three heat exchangers, ejector and feed pump. The ejector is equipped with a movable primary nozzle in order to optimize the axial position relative to the diffuser. At present the mechanism cannot be operated when the system is running, but in principle it could be modified for continuous adjustment during operation. An electronic expansion valve is used to control the liquid level in the evaporator based on overheating at the evaporator exit. The cooling load is provided by a supplementary heat exchanger where the chilled water is warmed up by the same ambient-temperature flow that cools the condenser.

The prototype is conceived with a "ready to market" structure. During components placing, several features had to be taken into account to permit easy connection with external water circuits, allow user access for assembly and disassembly operations and create a compact and moveable structure. A vertical arrangement was chosen for heat exchangers. This allowed reduction of space and mitigation of cavitation problems at the pump inlet. As a consequence, the main axis of ejector is vertical as well. Fig. 3 shows two pictures of the prototype. Note that the ejector depicted in the left image was a previous version, which is now substituted by the one shown on the right. A detailed description of the plant components (heat exchanger, pumps etc.) is given by Eames et al. (2013).

The working fluid is R245fa, which is selected because of its relatively high critical temperature, low system pressure ratio and, most importantly, positively sloped saturation vapour curve. Unfortunately, this fluid has a relatively high GWP, posing a potential limitation with respect to expected regulations on fluorinated gases. However, the growing ORC market has stimulated the formulation of low GWP alternatives matching the thermodynamic properties of R245fa, like HFO1233zd. Therefore, the findings presented herein retain their significance. About 50 kg of refrigerant are required for operation of the prototype, due to the large size of the heat exchangers.

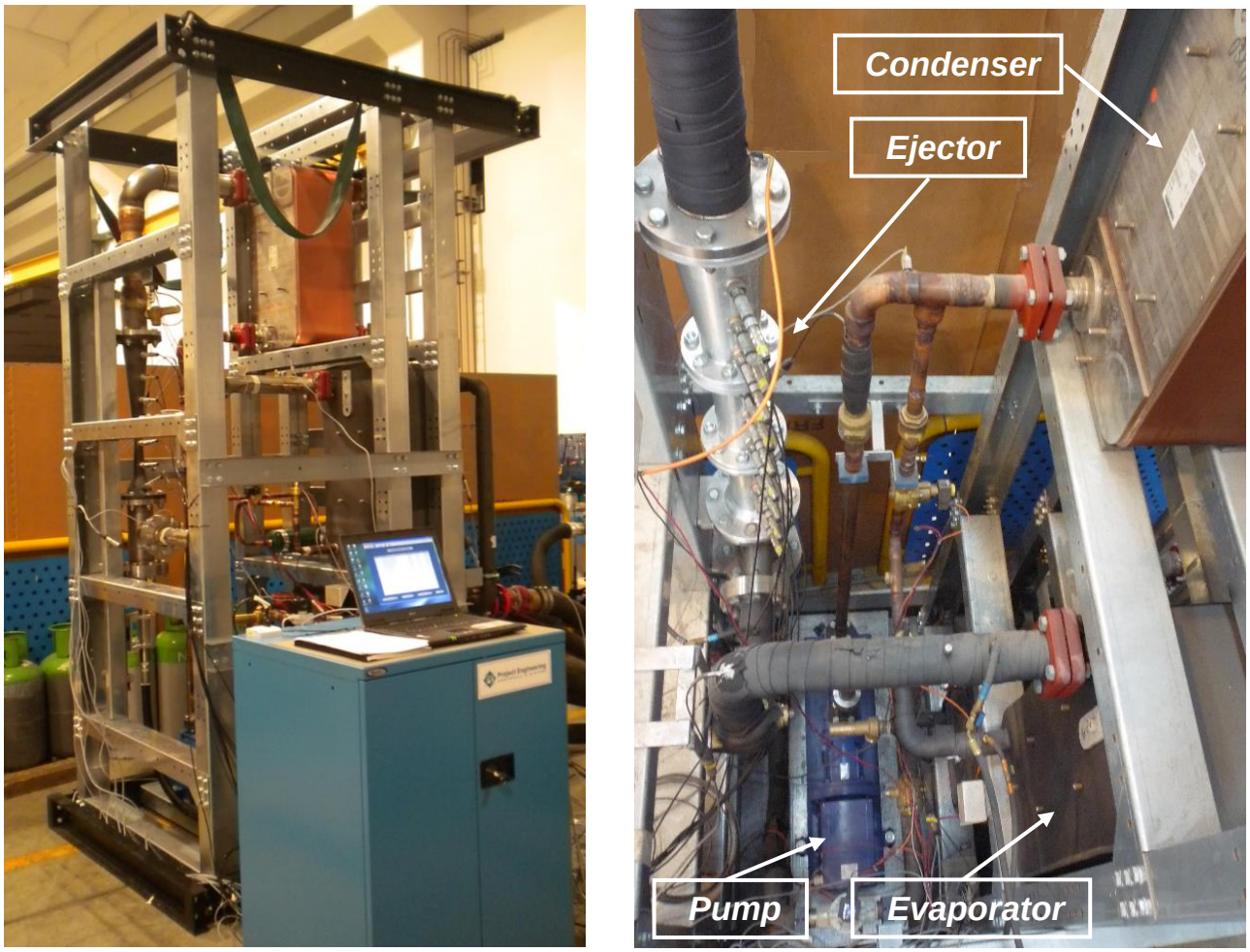

Fig. 3 – Views of the ejector chiller (note that the ejector is changed – present configuration on the right).

2.1. Ejector chiller design

The whole plant, including heat exchangers and piping, was designed using a numerical design tool developed by the authors. The code is based on a one-dimensional calculation method presented by Grazzini et al. (2012). The simulation allows for changes in several parameters in order to find the optimal cycle configuration (temperature and mass flow rates, superheating and subcooling levels, geometric features, etc.). Real fluid properties are used throughout the model by incorporating the NIST REFPROP subroutines (Lemmon et al., 2013).

The design code implements a routine for the design of the supersonic ejector profile. This is based on the CRMC (Constant Rate of Momentum Change) criterion by Eames (2002). The CRMC method is an attempt to reduce throat shock intensity by giving a prescribed momentum reduction rate throughout the mixing chamber and diffuser. The resulting profile is continuous and, from now on, it will be called supersonic diffuser or just diffuser. Two different ejectors were designed according to this code and tested. However, the performances obtained with the first two configurations were unsatisfactory (Eames et. al., 2013). Hence, the design concepts were reconsidered and a new ejector was manufactured. Fig. 4 shows the geometry of the ejector currently installed in the plant while its main geometrical parameters are summarized in Tab. 1.

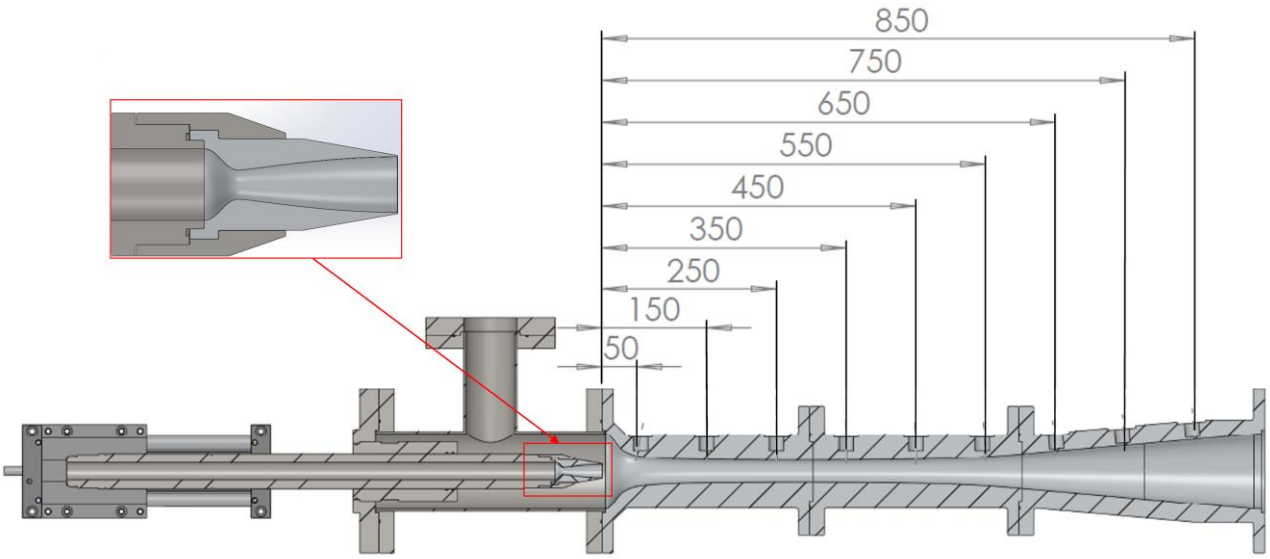

Fig. 4 – Currently installed ejector geometry

	Nozzle	Diffuser
Throat diameter [mm]	*10.2*	*31.8*
Exit diameter [mm]	*20.2*	*108.3*
Length [mm]	*66.4*	*950*
Material	Aluminum	Aluminum

Tab. 1 – Main geometrical parameters of the tested ejector

The new supersonic diffuser follows the CRCM criterion but has an increased length to improve mixing and pressure recovery (Milazzo et al., 2014). Numerical analyses on this third design showed that, for the set of operating conditions specified by the industrial partner, the primary nozzle was working under a high level of over-expansion. Therefore, two nozzles with a smaller exit area were simulated numerically and the results are presented in Fig. 5 (the related CFD scheme will be introduced later). As can be seen in the figure, a reduction of the nozzle exit area results in good improvements both in terms of entrainment ratio and critical pressure. The improved performance is due to a reduction in the expansion level of the primary flow, which is attained by matching the nozzle exit pressure with that of the mixing chamber.

Fig. 6 elucidates this concept by showing the static pressure field in the mixing chamber for two simulated cases. In the previous configuration (upper half of the figure), the primary flow expands down to very low exit pressures and shocks in order to reach the mixing chamber pressure. In the new configuration (lower half of the figure), the smaller pressure difference at the nozzle exit allows for a reduction in shock train intensities and pressure losses (the red spot marking a pressure above 2.5 bar in the upper part of Fig. 6 disappears in the lower part). This is also shown in Fig. 7 where the region with Mach number above unity is highlighted. The sonic line is much smoother in the new configuration and correctly follows the primary nozzle profile.

Based on these results, the nozzle design with exit diameter 20.2 mm was finally selected, manufactured and inserted in the ejector. In agreement with numerical analyses, substitution of the primary nozzle produced significant improvements and now chiller performance is aligned with or exceeds the results published by other authors (as will be shown later). This paper presents the experimental and numerical results obtained with this last design configuration (Fig. 4).

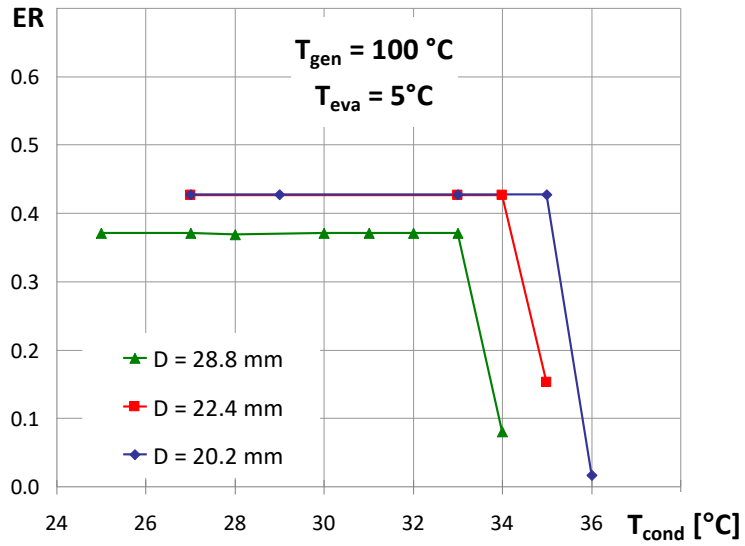

Fig. 5 – Entrainment Ratio for different values of the nozzle exit diameter

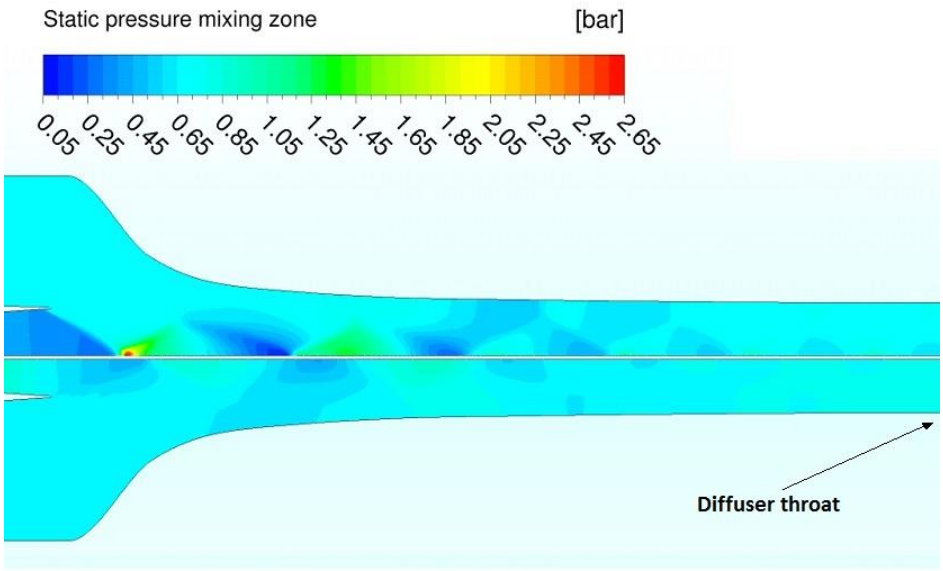

Fig. 6 – Static pressure in the mixing region for two different nozzle exit diameters: 28.8 mm (above the axis) and 20.2 mm (below the axis)

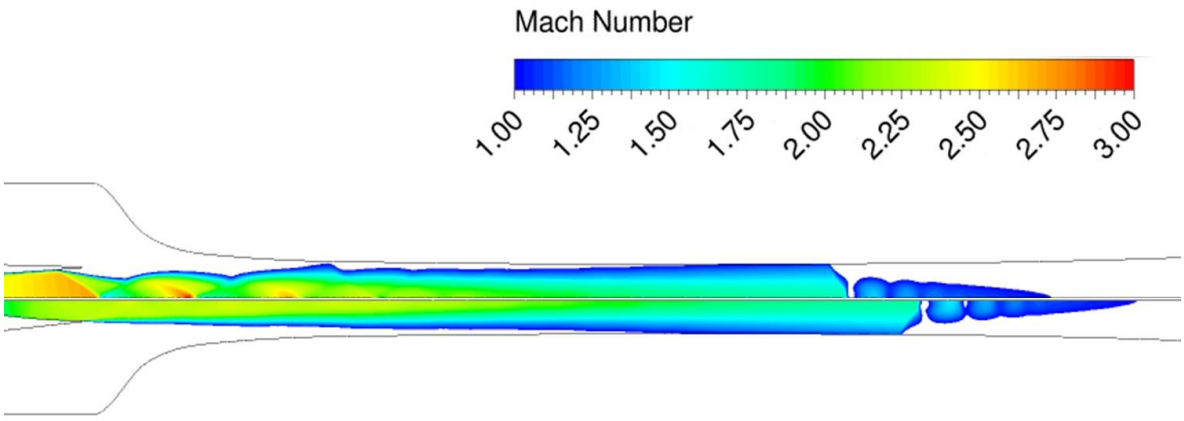

Fig. 7 – Supersonic Mach field along the diffuser for two different nozzle exit diameters: 28.8 mm (above the axis) and 20.2 mm (below the axis)

2.2. Instrumentation

Temperature measurements are obtained by resistance temperature detectors Pt100 whose precision class is 1/10 DIN. The probes are placed at the inlet and outlet connection of each heat exchanger. Resistance values are read and converted by a National Instruments cFP-RTD-124 module. Piezoresistive pressure transducers produced by Keller are used to obtain pressure values. Two pressure probes are placed at the inlet and outlet connections of each plate heat exchanger, and nine along the ejector mixing chamber and diffuser. Data are read and converted by a National Instruments cFP-AI-111 module. Water mass flow measurements in the external circuit are carried out with Endress+Hauser Promag electromagnetic flow meters. Electric power consumption of the feeding pump is measured by an electronic wattmeter. Thus far, flow measurements inside the refrigeration plants are absent. This was made necessary by the choice of the refrigerant, in that R245fa is a non-polar fluid with very low viscosity for which the use of expensive Coriolis mass flow meters is mandatory. Therefore, heat fluxes and refrigerant mass flow rates are measured by equivalence with the thermal fluxes flowing through the external water circuit. Due to this indirect method of measuring the mass fluxes, steady conditions are always sought to assure equality between water and refrigerant thermal fluxes. Nonetheless, the lack of direct mass flow measurement can lead to low accuracy of the experimental data. Hence, an extensive and detailed uncertainty analysis was performed to understand the level of confidence in the measurements.

2.3. Measurement uncertainty

The basic ideas of measurement uncertainty are well explained by many authors (Taylor, 1997; Figliola and Beasley, 2000; Moffat, 1988). Here we follow the more specific procedure referred to as “multiple sample” or “multiple measurement” uncertainty analysis. All uncertainties are evaluated with a confidence level of 95%. Bias or systematic errors are calculated by summing up the contribution stated by the manufacturers for both the instruments and data acquisition system. Tab. 2 summarizes the final level of accuracy for each measured quantity. During data acquisition, each experimental point is obtained by averaging over a period longer than the longest period contained in the signal waveform. This is done in order to avoid interference errors (Figliola and Beasley, 2000). The “precision index” or “random errors” are evaluated by taking the “standard deviation of the mean” for each measured quantity. The total uncertainty for each measured quantity is thus given by:

$$U_{95\%} = \sqrt{(B)^2 + (t_{v,95}P)^2} \tag{3}$$

Where B is the total bias or systematic error for the measured quantity, P is the precision index or random error for the measured quantity, $t_{v,95}$ is the “Student’s *t* estimator” and v are the number of acquisitions. Rigorously, v should be the number of degrees of freedom and the *t* estimator should be evaluated by the Student’s *t* distribution. However, when the number of acquisitions is higher than ~60 (as in our tests) the *t* estimator can be considered $t_{v,95} = 2$ and the difference between the degrees of freedom and the number of acquisitions can be safely neglected.

Error propagation for “derived quantities” (powers, mass flows, and enthalpies) is evaluated by square summation of the various “sensitivity indexes” (sometimes called partial uncertainties):

$$U_{95\%-derived} = \pm\sqrt{\sum_i \left(\frac{\partial R(x_i)}{\partial x_i} \cdot \delta x_i \right)} = \pm\sqrt{\sum_i \left(\theta_i \cdot \delta x_i \right)} \tag{4}$$

Where $R(x_i)$ is the "derived quantity", which is a function of several "measured quantities" x_i (e.g. temperature, pressure, etc…); θ_i is the sensitivity index, which represents the variation of the derived quantity subject to a variation δx_i of the measured quantity.

In the absence of an analytical formulation for the derived quantity (e.g., when evaluating the enthalpy of the refrigerant through NIST libraries), the sensitivity indexes are evaluated by "sequential perturbation" of the result (Moffat, 1988), that is, by numerically evaluating the sensitivity index as follows:

$$\frac{\partial R(x_i)}{\partial x_i} = \frac{1}{2}\left(\left|\frac{R(\bar{x}_i + \delta x_i) - R(\bar{x}_i)}{\delta x_i}\right| + \left|\frac{R(\bar{x}_i) - R(\bar{x}_i - \delta x_i)}{\delta x_i}\right|\right) \quad (5)$$

Where $\bar{x}_i$ is the average of the *i*-th "measured quantity" on which the "derived quantity" $R(x_i)$ depends.

The experimental error obtained for derived quantities such as mass flow rates, ER and COP depend on the working conditions and are reported graphically in the results presented in section 4.

Instrument	Model	Equipped component	ADC module	Total uncertainties
Piezoresistive pressure transducer	PA25HTT 0-30bar	Diffuser	cFP-AI-111	±(0.1% + 0.22% FS)
	PR23R 0.5-5bar	Evaporator	cFP-AI-111	±(0.1% + 0.22% FS)
	PA21Y 0-30bar	Generator, Condenser	cFP-AI-110	±(0.08% + 1% FS)
Resistance temperature detectors	Pt100	Whole plant	cFP-RTD-124	±0.25°C
Electromagnetic water flow meters	Promag 30F	Evaporator	cFP-AI-111	±(0.22% + 0.06% FS)
	Promag 50P	Generator	cFP-AI-111	±(0.5% + 0.04% FS)
	Promag 50W	Condenser	cFP-AI-111	±(0.5% + 0.04% FS)

Tab. 2 – Instrumentation total uncertainty

3. Numerical modelling

Simulations are performed using the commercial CFD package ANSYS FLUENT v14.5, which is based on a finite volume approach. The numerical model is based on the standard Navier-Stokes equations for compressible flows. Spatial discretisation of both the conservation and turbulence equations is second order accurate. The convective and diffusion terms are discretised following an upwind and central difference scheme respectively; gradients are evaluated by a least square approach. Due to the high Mach numbers in the flow field, a density-based implicit solver is used (Ansys, 2012). Convergence of the solution is defined by an error in the mass flow imbalance of less than 10^{-5} kg/s and calculations are stopped when all residuals are stable. Boundary conditions are equal to experimental data and are provided as total pressure and static temperatures at inlets, static pressure at outlet. Walls are assumed to be adiabatic.

Based on successful implementations reported in the literature (Menter et al., 2003; Bartosiewicz et al., 2003, 2005), a $k\omega$ SST turbulence model is selected for all simulations. The Ansys Fluent version of this model adopts what is called "Enhanced Wall Treatment" (EWT). This kind of near-wall treatment combines the standard low-Reynolds approach for fine near-wall meshes with "enhanced wall functions" for regions with coarser refinement. Hence, the need for tailoring the grid to a prescribed range of $y+$ (e.g., <1 for wall resolution or >15 for wall functions) is no longer urgent (Menter et al., 2003; Ansys, 2012). Nevertheless, the

grid was designed to have $y+$ values always less than 1 along the supersonic diffuser wall, where strong pressure gradients occur due to high back pressure and the presence of shocks.
Fig. 8 shows the computational domain while in Fig. 9 a detail of the numerical grid in the proximity of the primary nozzle trailing edge is represented. Due to the high directionality of the flow (axial velocity component always much greater than the transversal component), a structured grid is selected. This allows for longitudinal stretching of the elements, thus reducing the grid size. It should be noted that the nozzle trailing edge is simulated by accounting for the real thickness of the piece (curvature radius around 0.2 mm). This is an important feature because the development of the mixing layer is highly influenced by the wake formation behind the nozzle trailing edge.

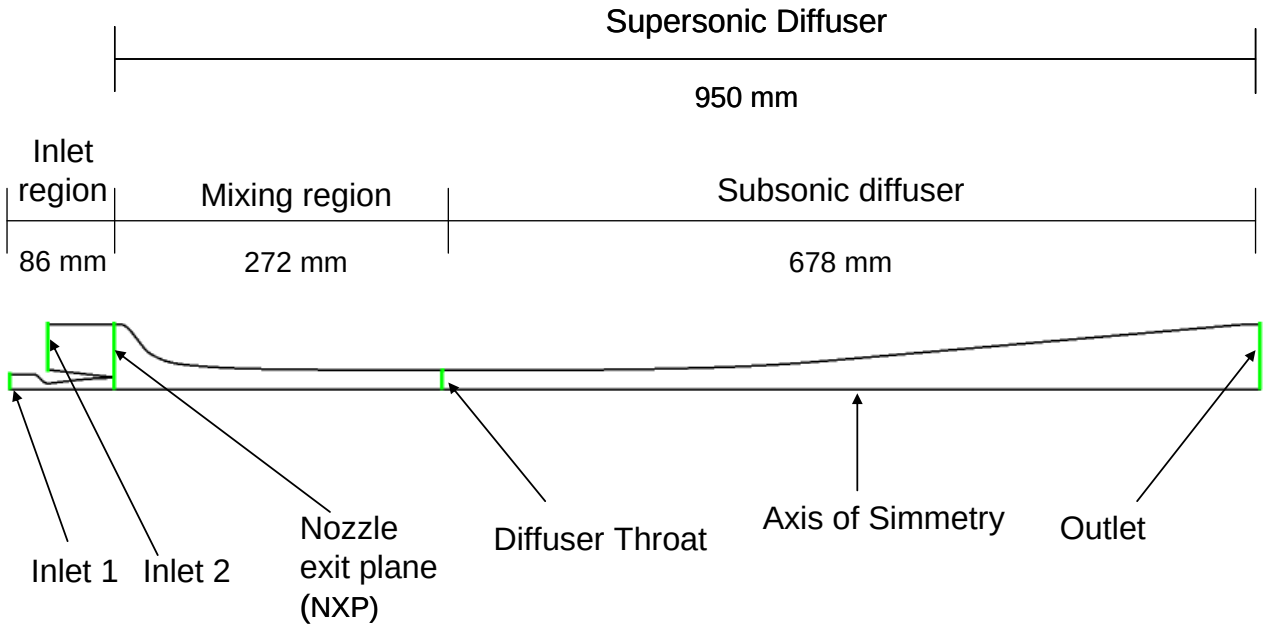

Fig. 8 – Computational domain

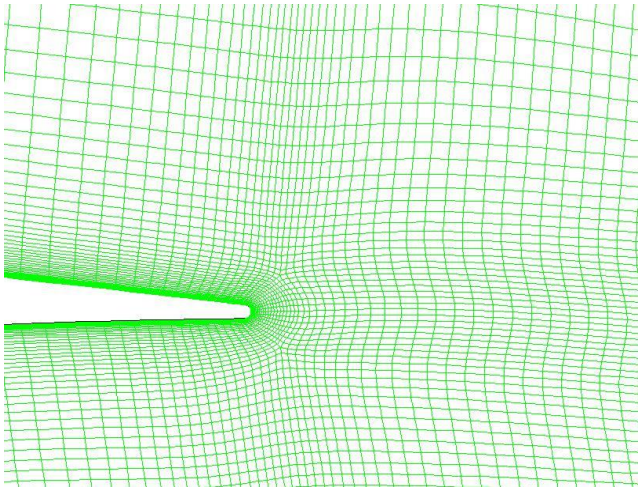

Fig. 9 – Detail of the numerical grid near the primary nozzle trailing edge

Grid dependence was checked by comparing the results of three grids with approximately 40 000, 80 000 and 150 000 cells. Convergence was reached for the grid of intermediate size. The maximum error in the prediction of the mass flow rate is found to be less than 0.1% with respect to the finest grid. Furthermore, the internal flow field was checked and resulted in negligible discrepancies, except for very small differences in the proximity of the diffuser shock. This is shown in Fig. 10 in terms of Mach number along the diffuser

axis. It should be noted that the numerical model predicts the formation of a shock train along the diffuser (the region highlighted in Fig. 10). This is sometimes referred as "pseudo-shock" and is due to the presence of thick boundary layers and high Mach numbers before the shock (Matsuo et al., 1999).
All calculations are performed by accounting for real gas properties of the refrigerant. The choice of a fluid with a positively sloped saturation curve (such as the R245fa), highly simplifies the ejector dynamics by avoiding the need for modelling a two phase and possibly metastable flow. Initially, properties were evaluated by means of the NIST libraries integrated within Fluent. However, this resulted in a very low convergence rate of the solution. Moreover, the stability of the calculations was weak. This was probably caused by a restricted range of validity of the NIST libraries, which caused the solution to fall in regions where the fluid properties are not defined (this is accentuated during the first iterations where the calculations are highly oscillating). Hence, an algebraic Peng-Robinson equation of state (EOS) was implemented. This is a relatively simple procedure in Fluent, as it provides for a template Peng-Robinson model which just needs the specific refrigerant parameters to be input. A description of the EOS parameters for the R245fa refrigerant can be found in Lujan et al. (2012). The impact of the algebraic EOS was analysed by comparison with results obtained by use of the NIST libraries and ideal gas approximation. In terms of mass flow rates the difference between the NIST libraries and Peng-Robinson is always below 1%, while is larger than 6% for the ideal gas approximation. The local field was also checked and results are given in Fig. 11.

In conclusion, the main features of the numerical scheme can be summarized as follows:

- second order accurate discretisation scheme coupled with a density-based implicit solver,
- $k\omega$ SST turbulence model with Enhanced Wall Treatment,
- structured grid of around 80k elements with $y+$ values less than 1 at the supersonic diffuser wall,
- primary nozzle simulated accounting for the real thickness of the trailing edge,
- real gas properties simulated by means of a third order Peng-Robinson state equation,
- adiabatic walls.

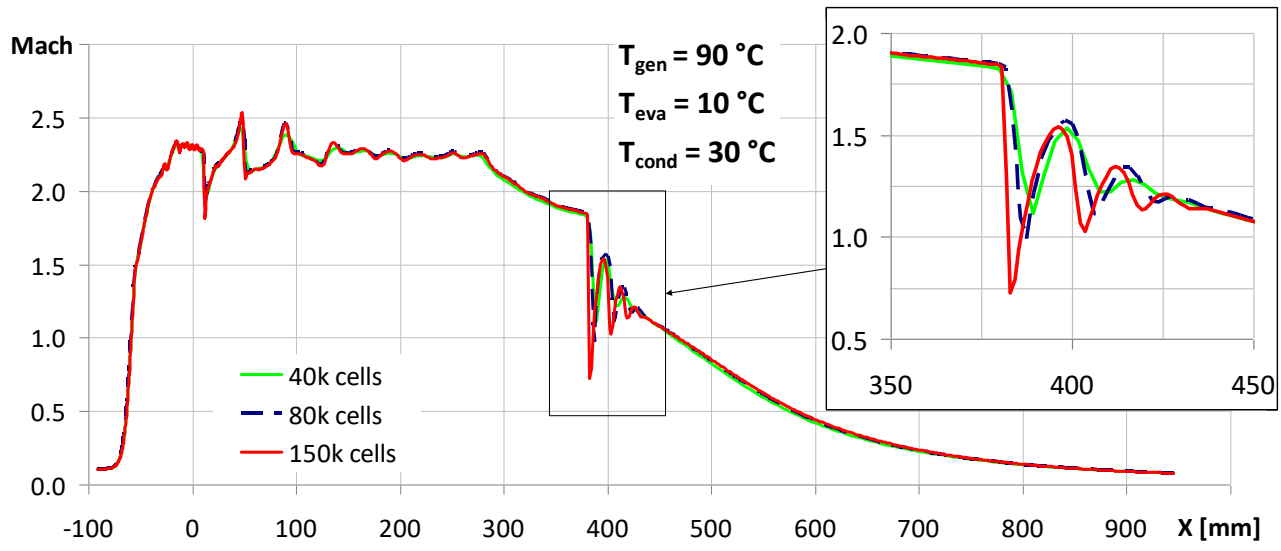

Fig. 10 – Grid dependence for the Mach number profile along the ejector axis.

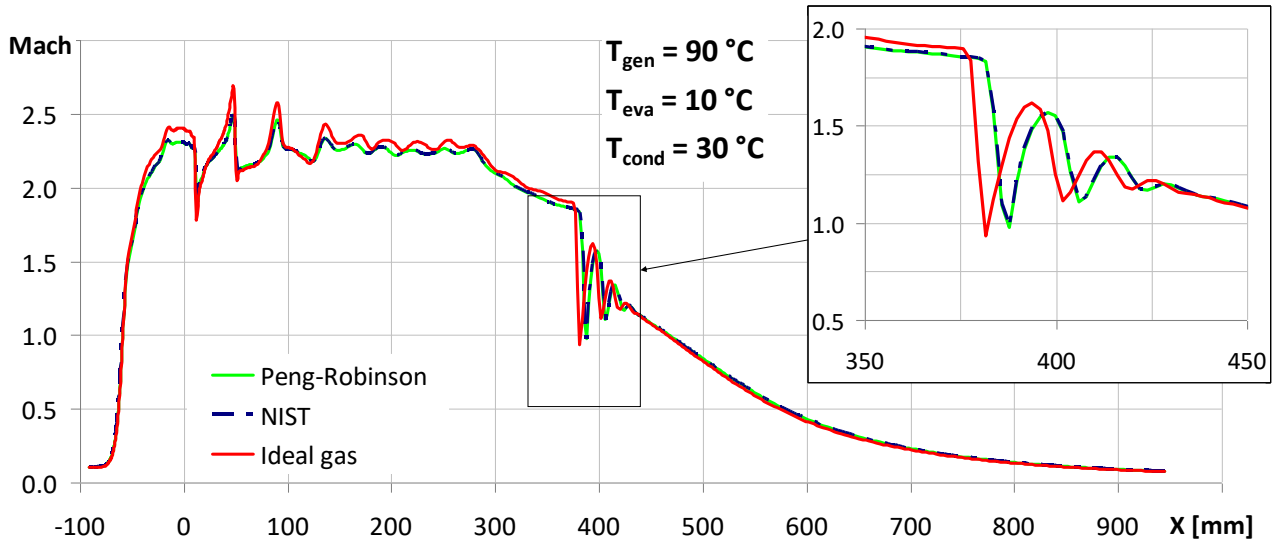

Fig. 11 – EOS sensitivity for the Mach number profile along the ejector axis

4. Results and discussion

Fig. 12 shows the experimental results of the refrigerator in terms of Coefficient Of Performance (COP). The generator temperature is around 90°C which is a temperature suitable for solar cooling or waste-heat recovery applications. Two levels of evaporator temperature are selected which represent standard values for air conditioning. 5°C superheating is set at the evaporator exit. Only few operating points are reported herein among the large amount of data gathered in hours of operation. This was due to the difficulty to achieve stable boundary conditions for a suitable period of time in a real industrial environment.

As can be seen in Fig. 12, the COP reached by the system is well above 0.4 when evaporating at 5°C and around 0.55 when evaporating at 10°C. These levels are not too far from those obtained by single-effect absorption chillers and match or exceed the performance obtained by other authors (Chen et al. 2013). However, the value of critical condenser temperature is below 30°C (saturation temperature), which means that the energy content of the primary flow is mainly exploited to draw in a consistent amount of secondary flow. Nevertheless, some improvements may be reached by reducing the amount of friction losses inside the ejector. To this aim, numerical simulations have been conducted to analyse the impact of wall roughness on the global and local variables.

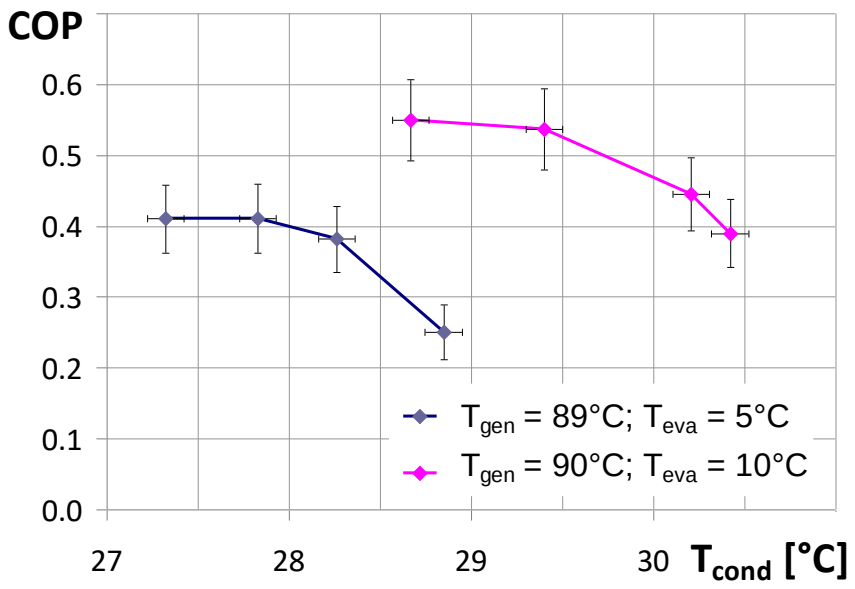

Fig. 12 – Ejector refrigerator COP

For historical reasons, the commonly used roughness definition in fluid dynamics is what is called the "uniform sand-grain roughness height", K_{sg}. Early experiments on friction losses performed by Nikuradse (1937) were obtained by covering pipe surfaces with a monolayer of uniform sand grains. Subsequently, Moody made use of Nikuradse's results to derive his chart (Moody, 1944). As a consequence, roughness height is defined as the mean diameter of the sand grains that cover the surface. This value is what is to be input in Ansys Fluent (Ansys, 2012). However, the "sand-grain" roughness is a completely different quantity from what is measured by any profilometer. These latter usually return some average of the surface vertical displacement, i.e. the arithmetic average height, K_a, or the root mean square height, K_{rms}.

Unfortunately, there is no exact conversion factor to transform a measured average roughness (arithmetic or root mean square) into an equivalent value of uniform sand grain roughness. A recent work from Adams et al. (2012) estimated theoretically the conversion factors and found that $K_{sg} \sim 3\ K_{rms}$ (also found by Zagarola and Smits, 1998) and $K_{sg} \sim 5.9\ K_a$. By comparison with experimental data they showed that conversion factors are subject to large uncertainty and should always be regarded as indicative values. Nevertheless, they concluded that using the conversion factor is always a better approximation than to use none.

In this study, three different sets of calculations were carried out with "sand-grain" roughness heights of 2, 20 and 60 micron respectively, as well as a set of calculations with smooth surfaces. Results were compared with experiments in terms of both ER and pressure profiles in order to find the roughness height that fits the experimental data at best. This value was finally compared to the real roughness as measured inside the ejector to check for discrepancies.

The results in terms of ER are shown in Fig. 13. For low values of back pressures, i.e. when the ejector is in choked conditions, the differences in the predicted entrainment ratios are rather small for different roughness heights. The percentage difference between the smoothest and roughest cases is no greater than 4.5% and always less than 2.5% between the smooth and intermediate cases. As the condenser pressure increases, higher values of friction cause the critical state to appear in advance. This result is indeed expected, as greater friction translates into larger amounts of total pressure losses, thus reducing the capability of the mixed flow to withstand high values of back pressure. On the contrary, in the case of smooth surfaces, the simulated ejector manages to maintain choked conditions for higher temperatures at the condenser. This analysis highlights the importance of the manufacturing process on the performance of a supersonic ejector refrigerator. Friction losses are obviously neither the only, nor the greatest source of losses inside the ejector (e.g. large losses come from shock, recirculations and mixing losses). Nevertheless, with a relatively small

economic outlay (i.e. by polishing the internal surfaces) significant advantage can be gained. Finally, it can be noted that the presence of friction also influences the steepness and extension of the off-design regime. A higher level of roughness causes a slower reduction of the secondary mass flow with respect to back pressure increases. As a consequence the range of "non-choked" operations becomes larger.
In Fig. 14 the same results are reported by singling out the curves related to the primary and secondary mass flows. As one could expect, the numerical error is mainly due to the prediction of the secondary flow rate. This might seem an obvious result, the flow within the primary nozzle being a simple 1D isentropic one. However, even for such "easy" flows, errors can arise from small differences in the geometrical dimensions of the nozzle (especially near the sonic throat) and from approximate evaluations of the fluid property (e.g. considering a constant gas specific heat ratio). In the present study the refrigerant was simulated by accounting for the real property of the fluid and the geometry of the primary nozzle was accurately checked before installation. As for the secondary flow, the error is larger, especially in off-design conditions. By inspection of the numerical curves it appears that a better agreement could be obtained by a slightly lower level of surface roughness. The calculated and measured data for the mass flow rates are reported in Tab. 3 and Tab. 4 together with the experimental and numerical error.

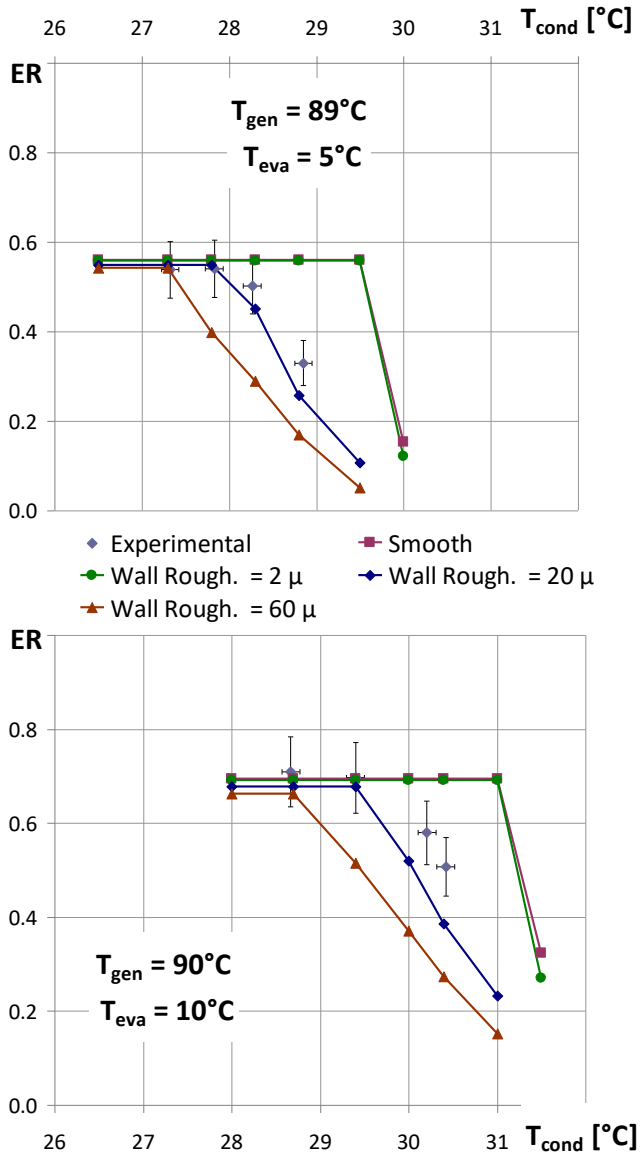

Fig. 13 – Experimental/numerical comparison of ejector Entrainment Ratio (ER) for different values of simulated wall roughness

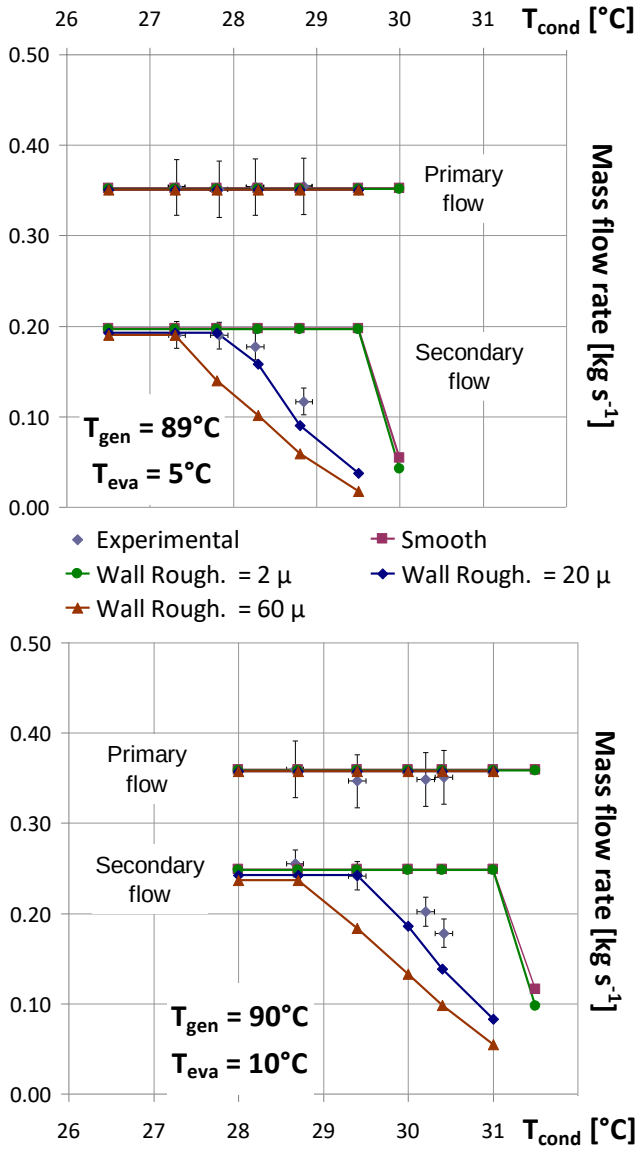

Fig. 14 – Experimental/numerical comparison of ejector primary (high curves) and secondary (low curves) mass flow rates for different values of simulated wall roughness

Fig. 15 and Fig. 16 show the comparison between the static pressures measured along the diffuser wall and the corresponding profiles obtained by numerical simulations. Clearly, the calculated pressure profiles are highly dissimilar for different roughness heights. In particular, the curves corresponding to smooth surfaces are very distant from the experimental data (this is obviously not true at the extremes of the curves in which the pressure boundary conditions are imposed as equal to the experimental data).

In much the same way as for the ER, the curve of intermediate surface roughness is the one that more closely reproduces the experimental data. Hence, it can be inferred that the equivalent sand grain roughness height, as predicted by numerical analysis, is close to 20 microns. Converting this value with the abovementioned conversion factors gives an estimated arithmetic roughness height of $K_a \sim 3.5$ microns.

The K_a roughness of the ejector internal surface was subsequently measured in different location by means of a Mahr contact surface profilometer. Resulting values of K_a ranged from 4 to 6 microns depending on the different measurement sites. Hence, it is concluded that the roughness height predicted by numerical analysis fall somewhat below the range of the experimental data. However, the error can be considered negligible on

accounting for the large uncertainty in the conversion factor and the approximation introduced by the numerical and experimental methods.

Case	Saturation Temperature [°C]			Mass flow rates [kg s^{-1}]			Error with experiments [%]		
	generator	evaporator	condenser	generator	evaporator	condenser	generator	evaporator	condenser
Experimental	*89.0*	*5.0*	*27.3*	*0.35 ± 0.03*	*0.19 ± 0.01*	*0.53 ± 0.05*	/	/	/
	89.1	*5.1*	*27.8*	*0.35 ± 0.03*	*0.19 ± 0.01*	*0.53 ± 0.05*	/	/	/
	89.3	*5.3*	*28.3*	*0.35 ± 0.03*	*0.18 ± 0.01*	*0.52 ± 0.05*	/	/	/
	89.6	*5.0*	*28.8*	*0.35 ± 0.03*	*0.12 ± 0.01*	*0.47 ± 0.04*	/	/	/
numerical smooth	*89*	*5*	*27.3*	*0.352*	*0.197*	*0.549*	*0.4*	*3.5*	*4.1*
	"	*"*	*27.8*	*0.352*	*0.197*	*0.549*	*0.2*	*3.8*	*4.3*
	"	*"*	*28.3*	*0.352*	*0.197*	*0.549*	*0.4*	*11.1*	*6.2*
	"	*"*	*28.8*	*0.352*	*0.197*	*0.549*	*0.7*	*68.5*	*17.3*
numerical 2 μ	*89*	*5*	*27.3*	*0.352*	*0.196*	*0.548*	*0.5*	*3.2*	*3.9*
	"	*"*	*27.8*	*0.352*	*0.196*	*0.548*	*0.1*	*3.4*	*4.1*
	"	*"*	*28.3*	*0.352*	*0.196*	*0.548*	*0.5*	*10.7*	*6.0*
	"	*"*	*28.8*	*0.352*	*0.196*	*0.548*	*0.7*	*67.9*	*17.1*
numerical 20 μ	*89*	*5*	*27.3*	*0.351*	*0.193*	*0.544*	*0.7*	*1.3*	*3.1*
	"	*"*	*27.8*	*0.351*	*0.193*	*0.544*	*0.1*	*1.6*	*3.3*
	"	*"*	*28.3*	*0.351*	*0.158*	*0.509*	*0.7*	*10.8*	*1.5*
	"	*"*	*28.8*	*0.351*	*0.090*	*0.441*	*1.0*	*22.8*	*5.7*
numerical 60 μ	*89*	*5*	*27.3*	*0.351*	*0.190*	*0.541*	*0.8*	*0.0*	*2.6*
	"	*"*	*27.8*	*0.351*	*0.140*	*0.490*	*0.2*	*26.5*	*6.9*
	"	*"*	*28.3*	*0.351*	*0.102*	*0.452*	*0.8*	*42.7*	*12.5*
	"	*"*	*28.8*	*0.351*	*0.059*	*0.410*	*1.0*	*49.3*	*12.4*

Tab. 3 – Predicted mass flow rates and error with respect to experimental data (case with generator T =89°C and evaporator T = 5°C)

Case	Saturation Temperature [°C]			Mass flow rates [kg s^{-1}]			Error with experiments [%]		
	generator	evaporator	condenser	generator	evaporator	condenser	generator	evaporator	condenser
Experimental	*89.8*	*9.9*	*28.7*	*0.36 ± 0.03*	*0.26 ± 0.01*	*0.60 ± 0.05*	*/*	*/*	*/*
	89.9	*9.9*	*29.4*	*0.35 ± 0.03*	*0.24 ± 0.02*	*0.58 ± 0.08*	*/*	*/*	*/*
	89.9	*10.0*	*30.2*	*0.35 ± 0.03*	*0.20 ± 0.02*	*0.56 ± 0.09*	*/*	*/*	*/*
	90.0	*9.8*	*30.4*	*0.35 ± 0.03*	*0.18 ± 0.02*	*0.54 ± 0.09*	*/*	*/*	*/*
numerical smooth	*90*	*10*	*28.7*	*0.359*	*0.249*	*0.608*	*0.4*	*2.6*	*0.8*
	"	*"*	*29.4*	*0.359*	*0.249*	*0.608*	*3.4*	*2.9*	*4.2*
	"	*"*	*30*	*0.359*	*0.249*	*0.608*	*2.9*	*23.1*	*8.4*
	"	*"*	*30.4*	*0.359*	*0.249*	*0.608*	*2.1*	*39.7*	*13.4*
numerical 2 µ	*90*	*10*	*28.7*	*0.358*	*0.248*	*0.606*	*0.5*	*2.9*	*0.6*
	"	*"*	*29.4*	*0.358*	*0.248*	*0.606*	*3.3*	*2.5*	*3.9*
	"	*"*	*30*	*0.358*	*0.248*	*0.606*	*2.8*	*22.7*	*8.2*
	"	*"*	*30.4*	*0.358*	*0.248*	*0.606*	*2.0*	*39.1*	*13.1*
numerical 20 µ	*90*	*10*	*28.7*	*0.358*	*0.242*	*0.600*	*0.7*	*5.1*	*0.5*
	"	*"*	*29.4*	*0.358*	*0.242*	*0.600*	*3.0*	*0.3*	*2.8*
	"	*"*	*30*	*0.358*	*0.186*	*0.544*	*2.6*	*8.0*	*3.0*
	"	*"*	*30.4*	*0.358*	*0.138*	*0.496*	*1.8*	*22.5*	*7.5*
numerical 60 µ	*90*	*10*	*28.7*	*0.357*	*0.237*	*0.594*	*0.8*	*7.3*	*1.5*
	"	*"*	*29.4*	*0.357*	*0.184*	*0.541*	*3.0*	*24.0*	*7.3*
	"	*"*	*30*	*0.357*	*0.133*	*0.490*	*2.5*	*34.4*	*12.6*
	"	*"*	*30.4*	*0.357*	*0.098*	*0.455*	*1.7*	*45.1*	*15.1*

Tab. 4 – Predicted mass flow rates and error with respect to experimental data (case with generator T =90°C and evaporator T = 10°C)

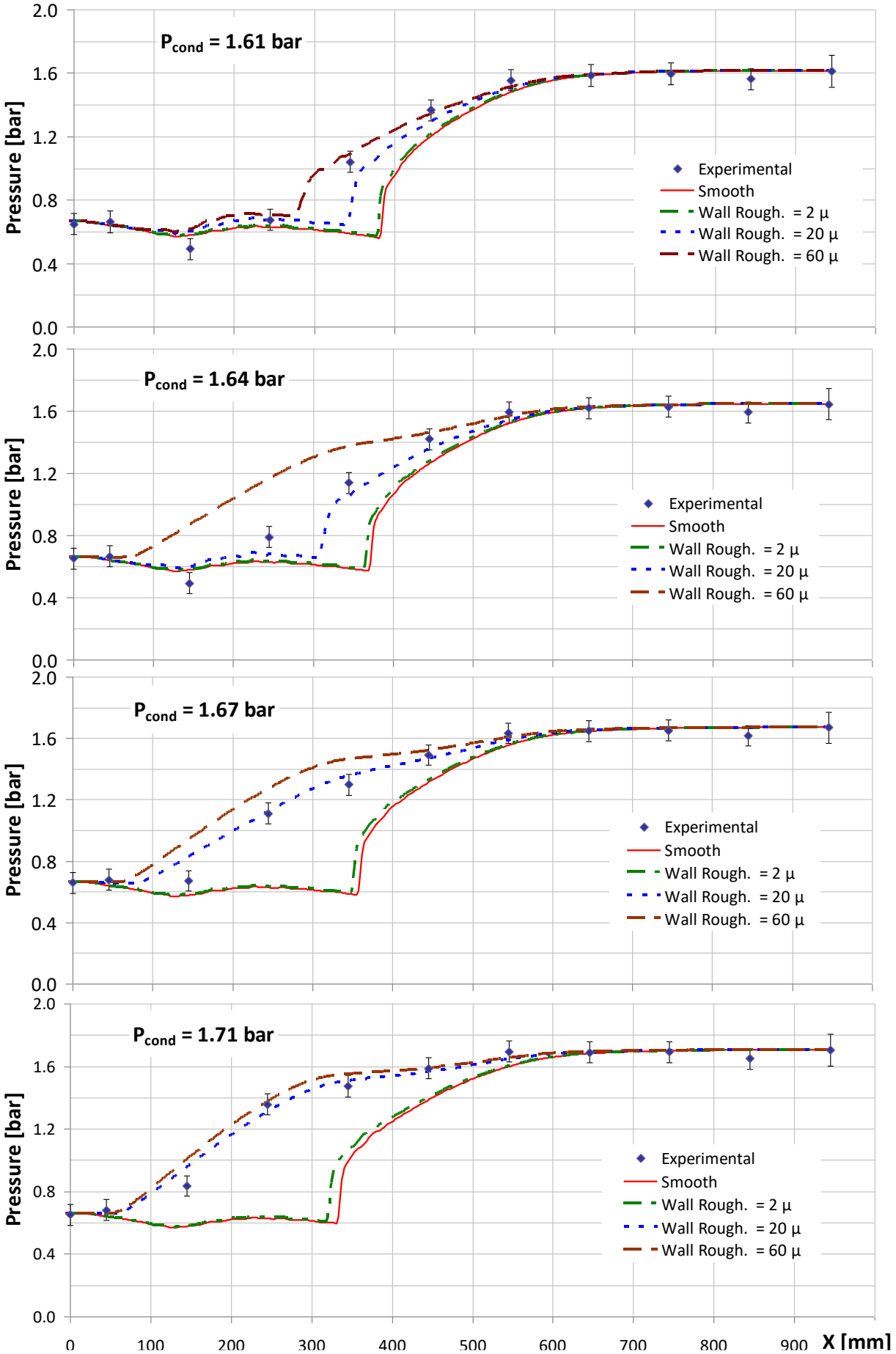

Fig. 15 – Experimental/numerical comparison of ejector pressure profiles for different values of simulated wall roughness case T generator = 89 °C and T evaporator = 5 °C

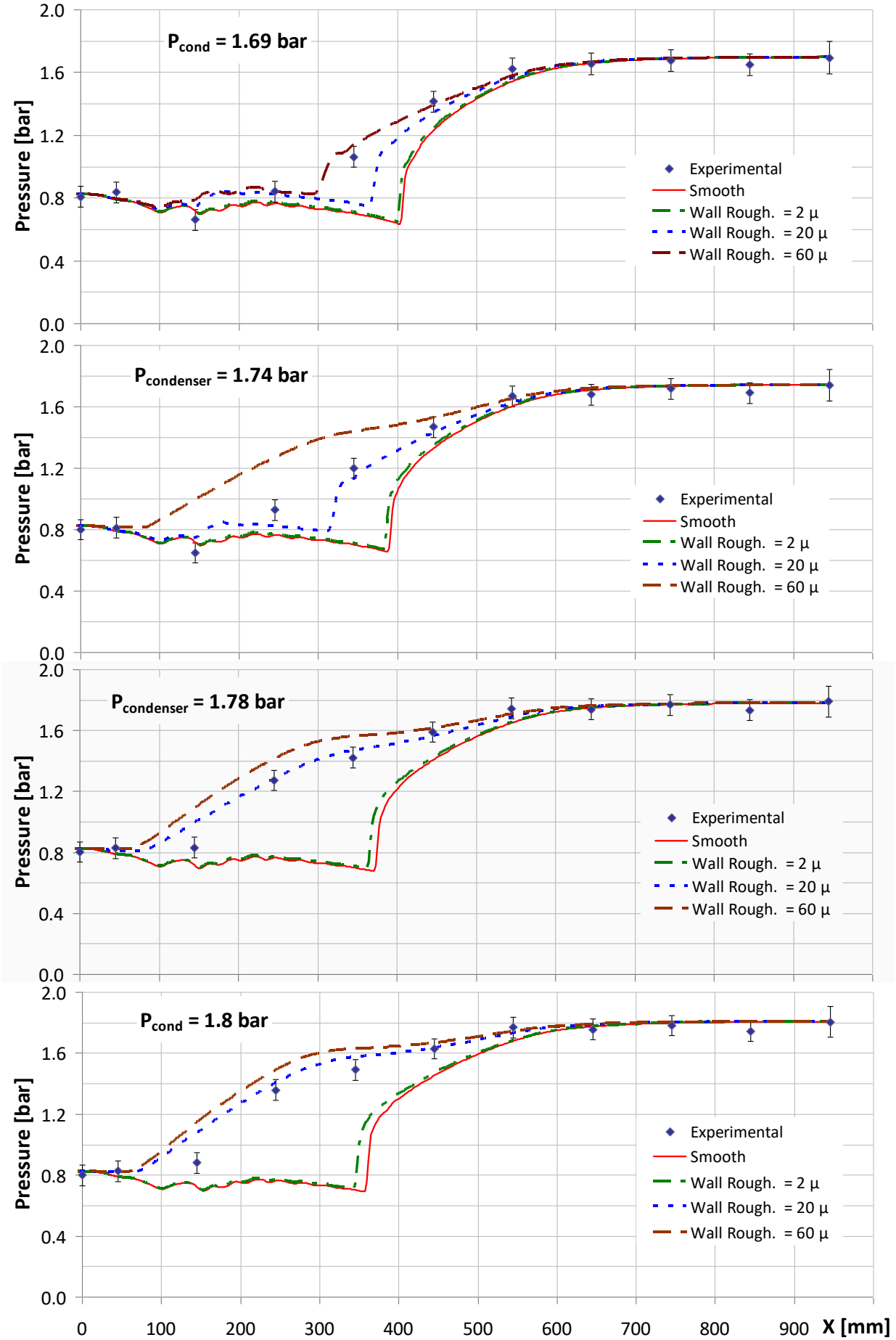

Fig. 16 – Experimental/numerical comparison of ejector pressure profiles for different values of simulated wall roughness case T generator = 90 °C and T evaporator = 10 °C

In conclusion, it is seen from the presented results that the agreement with experimental data is satisfactory both in terms of global and local parameters. The reasons for this success are to be found in the numerical scheme characteristics (see section 3). In particular, being the whole dynamics influenced by phenomena occurring within and outside the boundary layer (e.g. kinetic energy dissipation, detachment or thickening caused by shock interaction or adverse pressure gradients, etc…) the accuracy in the near-wall modelling and in friction evaluation is fundamental. Moreover, the secondary flow entrainment is highly influenced by the formation and evolution of the free shear layer behind the primary nozzle trailing edge. Hence, in order to correctly predict the amount of suction flow drawn into the ejector, accounting for the real trailing edge thickness is important. Lastly, the choice of refrigerant played an important role: the absence of condensation phenomena allows for the adoption of simple but reliable real-gas equations of state. Furthermore, complex phenomena that occur for two-phase supersonic flow (such as condensation shock or metastable states - Wegener and Mack, 1958) and impact pressure and temperature profiles are avoided.

5. Concluding remarks

The study presents the experimental and numerical results obtained on a supersonic ejector chiller working with R245fa as a refrigerant. The refrigerator is being developed and tested as part of a project cooperation between Frigel s.p.a and DIEF (Department of Industrial Engineering, University of Florence). Results were obtained for operating conditions which are typical in air conditioning and waste-heat recovery applications (generator and evaporator temperature around 90°C and 5-10°C respectively). An extensive numerical campaign was performed which resulted in very close agreement with experimental data both in terms of global and local parameters.

The main results of the present study can be summarized as follows:

- After reconsideration of the ejector design, the system reached quite high levels of COP, similar or greater than those published by other authors and not too far from those obtained by single effect absorption systems;
- The value of critical condenser temperature is unfortunately not as high. However, some improvements may be reached by reducing the amount of friction losses inside the ejector;
- Whereas the entrainment ratio at on-design (chocked) conditions is not significantly influenced by wall friction, on the other hand friction losses have a large impact on the onset of the off-design (non-choked) regime, thus reducing the critical pressure;
- Very close agreement between experimental and numerical data can be achieved both at on-design and off design conditions, provided that the impact of wall roughness is correctly evaluated;
- The success of the simulations in correctly predicting experimental data should be ascribed to the numerical scheme accuracy in modelling the near-wall dynamics, friction, geometrical features and real gas properties.

In order to achieve economic and technological feasibility of ejector chillers for industrial exploitation, more needs to be done to reach an adequate level of efficiency and make the cycle competitive with absorption systems. For this purpose, correct design of the ejector aerodynamic profile is most important and can be achieved by a numerical optimization procedure which couples a robust CFD solver with an appropriate search algorithm. This is currently under study by our research group and will be the object of a future article.

Acknowledgement

The authors wish to thank Michele Livi and Frigel s.p.a. for their support in the experimental activity.

References

Adams, T., Grant, C., Watson, H., 2012. A Simple Algorithm to Relate Measured Surface Roughness to Equivalent Sand-grain Roughness. Int. J. Mech. Eng. and Mechatron. 1, 66-71

Addy A.L., Dutton, J.C., Mikkelsen, C.D., 1981. Supersonic ejector–diffuser theory and experiments. Report No. UILU-ENG-82-4001. Department of Mechanical and Industrial Engineering, University of Illinois, Urbana-Champaign, Urbana, Illinois, USA

Ansys fluent theory guide, release 14.5, 2012, ANSYS Inc., Canonsburg, PA.

Bartosiewicz, Y., Aidoun, Z., Desevaux, P., and Mercadier, Y., 2003. CFD-experiments integration in the evaluation of six turbulence models for supersonic ejectors modeling. Conference Proc., Integrating CFD and Experiments, Glasgow, UK

Bartosiewicz, Y., Aidoun, Z., Desevaux, P., Mercadier, Y., 2005. Numerical and experimental investigations on supersonic ejectors. Int. J. Heat and Fluid Flow 26, 56–70

Chen, X., Omer, S., Worall, M., Riffat, S., 2013. Recent developments in ejector refrigeration technologies. Renew. Sustain. Energy Rev. 19, 629–651.

Eames, I.W., 2002. A new prescription for the design of supersonic jet-pumps: the constant rate of momentum change method. Appl. Therm. Eng. 22, 121–31.

Eames, I.W., Milazzo, A., Paganini, D., Livi, M., 2013. The design, manufacture and testing of a jet-pump chiller for air conditioning and industrial application. Appl. Therm. Eng. 58, 234 – 240.

ESDU Ejectors and jet pumps Data item 86030, 1986. ESDU International Ltd, London, UK.

Figliola, R.S., Beasley, D.E., 2000. Theory and design for mechanical measurements, 3rd edition. John Wiley & Sons Inc., Hoboken, NJ.

Ginoux, J.J., 1973. Supersonic Ejectors, AGARDograph No.163. Available from NTIS, Springfield, Va.

Grazzini, G., Milazzo, A., Paganini, D., 2012. Design of an ejector cycle refrigeration system. Energy Convers. Manag. 54, 38–46.

Hemidi, A., Henry, F., Leclaire, S., Seynhaeve, J., Bartosiewicz, Y., 2009. CFD analysis of a supersonic air ejector. Part II: Relation between global operation and local flow features. Appl. Therm. Eng. 29, 1523–1531.

Lemmon, E.W., Huber, M.L., McLinden, M.O., 2013. NIST Standard Reference Database 23: Reference Fluid Thermodynamic and Transport Properties-REFPROP, Version 9.1. National Institute of Standards and Technology, Standard Reference Data Program, Gaithersburg, Maryland, USA.

Luján, J.M., Serrano, J.R., Dolz, V., Sánchez, J., 2012. Model of the expansion process for R245fa in an Organic Rankine Cycle (ORC). Appl. Therm. Eng. 40, 248–257.

Matsuo, k., Miyazato, Y., Heuy-Dong Kim, 1999. Shock train and pseudo-shock phenomena in internal gas flows. Progress in Aerospace Sciences 35, 33 – 100.

Menter, F., Ferreira, J.C., Esch, T., Konno, B., 2003. The SST Turbulence Model with Improved Wall Treatment for Heat Transfer Predictions in Gas Turbines. In: Proceedings of the International Gas Turbine Congress. Tokyo, Nov. 2003

Milazzo, A., Rocchetti, A., Eames, I.W., 2014. Theoretical and experimental activity on Ejector Refrigeration. Energy Procedia 45, 1245 – 1254.

Moffat, R.J., 1988. Describing the uncertainties in experimental results. Experimental Thermal and Fluid Science 1, 3-17.

Moody, L.F., 1944. Friction factors for pipe flow. ASME Trans. 66, 671–683.

Nikuradse, J. 1937. Laws of flow in rough pipes. NACA Technical Memorandum 1292

Ruangtrakoon, N., Thongtip, T., Aphornratana, S., Sriveerakul, T., 2012. CFD simulation on the effect of primary nozzle geometries for a steam ejector in refrigeration cycle. Int. J. Therm. Sci. 63, 133-145

Srikhirin, P., Aphornratana, S., Chungpaibulpatana, S., 2001. A review of absorption refrigeration technologies. Renew. Sustain. Energy Rev. 5, 343–372

Sriveerakul, T., Aphornratana, S. , Chunnanond, K., 2007. Performance prediction of steam ejector using computational fluid dynamics: Part 1. validation of the CFD results. Int. J. Therm. Sci. 46, 812–822.

Taylor, J.R., 1997. An introduction to error analysis, 2nd edition. University Science Books, Sausalito, CA.

Varga, S., Oliveira, A. C., Mab, X., Omer, S. A., Zhang, W., Riffat, S. B., 2011. Experimental and numerical analysis of a variable area ratio steam ejector, Int. J. Refrigeration 34, 668 – 675.

Wegener, P.P., Mack, L.M., 1958. Condensation in Supersonic and Hypersonic Wind Tunnels, in: Dreyden, H.L., Von Karman, Th., Advances in applied mechanics, Volume 5. Academic Press Inc., Publishers New York, pp. 307 – 340.

Zagarola, M.V., Smits, A.J., 1998. Mean-flow scaling of turbulent pipe flow. J. Fluid Mech. 373, 33-79.